


# Giant effective electron-magnon coupling in a nonmagnetic metal–ferromagnetic insulator heterostructure

Gaoyang Li,<sup>1</sup> Hao Jin,<sup>1,\*</sup> Yadong Wei,<sup>1</sup> and Jian Wang<sup>1,2,†</sup>

<sup>1</sup>College of Physics and Optoelectronic Engineering, Shenzhen University, Shenzhen 518060, China

<sup>2</sup>Department of Physics, The University of Hong Kong, Pokfulam Road, Hong Kong 999077, China

 (Received 10 February 2021; revised 18 March 2022; accepted 27 October 2022; published 10 November 2022)

Magnon-mediated spin transport across a nonmagnetic metal (NM) and ferromagnetic insulator (FI) interface depends critically on electron-magnon coupling. We propose a route to enhance electron-magnon coupling from a transport viewpoint. A theoretical formalism for magnon-mediated spin current is developed based on the nonequilibrium Green's function. In the language of transport, the effective electron-magnon coupling at the NM/FI interface is determined by the self-energy of the FI lead, which is proportional to the density of states (DOS) at the interface due to the nonlinear process of electron-magnon conversion. By tuning the interfacial DOS, the spin conductance of two-dimensional (2D) and 3D NM/FI systems can be significantly enhanced by almost three orders of magnitude, setting up a new platform of manipulating electron-magnon coupling.

DOI: [10.1103/PhysRevB.106.205303](https://doi.org/10.1103/PhysRevB.106.205303)

## I. INTRODUCTION

In conventional spin-current studies, pure spin current without an accompanying charge is generated in nonmagnetic metals (NMs). Since this spin current is carried by electrons, waste heat is inevitable. In 2010, it was found that a ferromagnetic insulator (FI) can conduct spin current in the form of magnons without Joule heating, and magnons can travel a long distance in yttrium iron garnet (YIG) [1], which survives even in the presence of disorders [2]. Since then, spin transport in FIs has become a topic of interest in spintronics.

In the presence of a temperature gradient across the NM/FI interface, the magnon-mediated spin Seebeck effect (SSE) [3,4] and the magnon-mediated spin Peltier effect (SPE) appear. The magnon-mediated SSE was understood in terms of spin pumping and was found to be proportional to spin-mixing conductance [5], while it was studied in the Pt/YIG bilayer using a linear-response theory [6]. Driven by the temperature gradient, rectification and a negative differential SSE were predicted, and rectification of the SPE was also discussed [7]. For a bilayer structure consisting of a paramagnetic metal and an FI, the magnon-mediated SPE was studied using nonequilibrium Green's function theory [8]. Other studies included the noise of spin current [9] injected by ferromagnetic resonance [1,10], the rectification effect of the SSE of a spin Seebeck engine [11], the proposal of optimal heat to a spin-polarized charge-current converter [12], the conversion of magnon current to charge and spin current in a Coulomb blockade regime [13], controlling spin Seebeck current using the Coulomb effect in a spin Seebeck device [14], and magnon-mediated electric current drag in a NM/FI/NM system [15,16]. The spin Peltier effect in a bilayer structure

(paramagnetic metal/FI) and the SSE in antiferromagnets and compensated ferrimagnets have also been studied theoretically [8,17].

The manifestation of all magnon-mediated spin-transport properties studied above depends critically on the magnitude of electron-magnon coupling at the NM/FI interface, which is very small due to the nonlinear process of electron-magnon conversion. In conventional wisdom, electron-magnon coupling is a static property and the optimal value can be obtained by searching for different materials or interfaces. However, in achieving multifunctionalities, one has to balance among different targeted properties in choosing the suitable material, which makes it difficult to optimize a single property. Efforts have been made to control the quality of the interface by avoiding the oxidization layer [18], changing surface roughness [19], and surface polishing [20]. Another strategy is to reduce the conductivity mismatch at the interface by inserting another layer of material [21,22], which has proven to be very successful. Large enhancement of the SSE through the NM/FI interface was demonstrated experimentally by inserting atomically thin magnetic or nonmagnetic metals, semiconductors, as well as layers of antiferromagnetic insulator (AFI) [19,20,23–28]. While reduction of interfacial conductivity mismatch is a general strategy, a new possibility in optimizing effective magnon-electron coupling on top of the bare electron-magnon coupling exists. This can be achieved from the transport viewpoint by increasing the interfacial density of states (DOS) at the NM/FI interface.

It is instructive to recall the electrochemical capacitance where quantum corrections to the classical capacitance can be important in nanoscale systems giving rise to quantum behavior [29–31]. For a parallel plate capacitor, these corrections are determined by the local DOS at the surfaces of two conductors due to the field penetration into the conductors. In contrast to the static DOS, this DOS is for the open system and hence it is dynamical [32]. As a result, the electrochemical

\*jh@szu.edu.cn

†jianwang@hku.hk

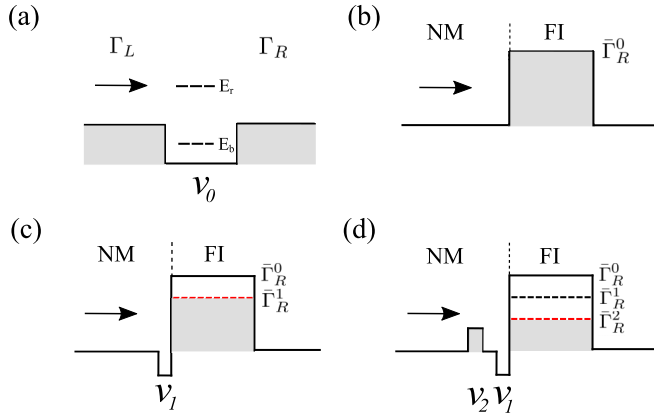


FIG. 1. (a) A tunneling structure where  $\Gamma$  describes the coupling between the scattering region and the lead. (b) The NM/FI interface is represented schematically by a barrier with an effective coupling constant denoted symbolically by  $\bar{\Gamma}_R^0 = D_0\Gamma_R$ . (c) Putting a potential well adjacent to the interfacial barrier gives rise to a large interfacial DOS  $D_1 > D_0$  and yields a larger effective coupling  $\bar{\Gamma}_R^1 = D_1\Gamma_R$ . Note that a larger  $\bar{\Gamma}_R$  corresponds to a larger electron-magnon coupling, and the effective barrier height is reduced (denoted by the red line). (d) Placing an additional barrier next to the well generates an even larger DOS  $D_2$  and effective coupling, which corresponds to an even smaller barrier height.

capacitance is no longer purely a geometrical quantity, but it can be influenced dynamically by the transport density of states.

As depicted in Fig. 1(a), scattering in a finite potential well ( $V_0 < 0$ ) can be modeled in the Breit-Wigner form [33,34]. For energy  $E < 0$ , bound states  $E_b$  may exist inside the potential well, while for energy  $E > 0$ , there are quasibound states  $E_r$  above the potential well [35–39]. Near the quasibound-state energy  $E = E_r$ , the transmission coefficient is given by

$$T = \frac{\Gamma_L\Gamma_R}{(E - E_r)^2 + (\Gamma_L + \Gamma_R)^2/4}, \quad (1)$$

where  $\Gamma_\alpha$  ( $\alpha = L, R$ ) is the linewidth function characterizing the coupling between the quasibound states and the  $\alpha$  lead with small  $\Gamma_\alpha$  corresponding to weak coupling. For a symmetric system with  $\Gamma_L = \Gamma_R = \Gamma$ , the transmission coefficient can reach 1 at resonance with the large DOS inside the potential well. Thus, in the language of transport, increasing the electron-magnon coupling amounts to increasing the linewidth function at the NM/FI interface. Due to the nonlinear process of electron-magnon conversion, the linewidth function of the FI lead (the right lead as shown in Fig. 2),  $\bar{\Gamma}_R$ , is the energy convolution of the DOS matrix at the NM/FI interface and the spectral function of the FI lead, denoted symbolically as  $\bar{\Gamma}_R^0 = D_0\Gamma_R$ , where  $D_0$  is the interfacial DOS and  $\Gamma_R$  is the spectral function of the FI lead. Therefore, the effective electron-magnon coupling is no longer a static (geometrical) quantity but is dressed by the transport DOS, and it can be changed by an incoming electron. By manipulating the interfacial DOS at the NM/FI interface, the effective electron-magnon coupling can be changed drastically. Since the electron-magnon coupling is very small, we model the

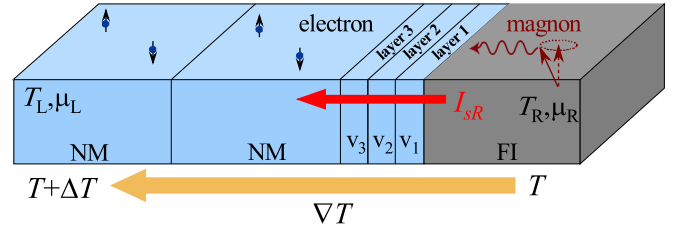


FIG. 2. Schematic illustration of the NM/NM/FI heterostructure and the magnon-mediated SSE. The central NM region is connected to a left NM lead and a right FI lead, whose temperatures are  $T_L$  and  $T_R$ , respectively. We define  $T_L > T_R$  with the temperature gradient  $\nabla T$ . The three layers in the central NM region adjacent to the NM/FI interface (labeled as layers 1, 2, and 3) are subjected to different on-site potentials ( $v_1$ ,  $v_2$ , and  $v_3$ , respectively). Electrons injected from the left lead travel through the three on-site potentials and are scattered back by magnons at the NM/FI interface. A magnon-mediated pure spin current  $I_{sR}$  is thus generated, which is illustrated by the red arrow.

interface by a barrier with a large barrier height [see Fig. 1(b)]. Placing a potential well next to the barrier, electrons are trapped in the well for a longer time, giving rise to a large interfacial DOS,  $D_1 > D_0$  [Fig. 1(c)]. This in turn increases the effective electron-magnon coupling, i.e.,  $\bar{\Gamma}_R^1 = D_1\Gamma_R$ , making the effective barrier height smaller and thereby increasing the magnon-mediated spin conductance. By putting an additional barrier next to the well [Fig. 1(d)], electrons can resonantly tunnel through the barrier and dwell in the well for an even longer time with a huge DOS. This yields a further increase of effective electron-magnon coupling and reduces the barrier height, which results in a significant enhancement of the spin conductance. Indeed, in calculating magnon-mediated spin conductance driven by temperature for an ideal two-dimensional (2D) and 3D NM/FI nanoribbon (nanowire), a giant enhancement of spin conductance with almost three orders of magnitude is achieved by modifying the interfacial DOS. This opens up a new window of engineering the effective electron-magnon coupling at the NM/FI interface by changing the system parameters.

## II. THEORETICAL FORMALISM

Figure 2 shows a schematic of the heterostructure. We consider a system consisting of a central NM scattering region, a left NM lead, and a right FI lead. The Hamiltonian of the system ( $\hbar = e = 1$ ) is given by

$$H = H_L + H_R + H_d + H_T + H_{sd}, \quad (2)$$

where

$$H_L = \sum_{k\sigma} \epsilon_{k\sigma,L} c_{k\sigma}^\dagger c_{k\sigma} \quad (3)$$

is the Hamiltonian of the left lead. Operator  $c_{k\sigma}^\dagger$  ( $c_{k\sigma}$ ) creates (annihilates) an electron with momentum  $k$  and spin  $\sigma$  in the left lead. The right lead can be described by a Heisenberg lattice. In the large spin limit or at low temperature, it can be mapped into magnon gas by using the Holstein-Primakoff transformation [40]. Therefore, the right lead Hamiltonian is

approximated expressed as

$$H_R = \sum_q \omega_q a_q^\dagger a_q. \quad (4)$$

Operator  $a_q^\dagger$  ( $a_q$ ) creates (annihilates) a magnon with momentum  $q$  in the right FI lead, and  $\omega_q$  is magnon dispersion of the FI lead. The Hamiltonian of the central NM region is

$$H_d = \sum_{n\sigma} (\epsilon_{n\sigma} + V) d_{n\sigma}^\dagger d_{n\sigma}, \quad (5)$$

where  $d_{n\sigma}^\dagger$  ( $d_{n\sigma}$ ) creates (annihilates) an electron in level  $n$  of the central region with spin  $\sigma$ .  $V$  is an on-site potential applied to manipulate the system spin transport. The coupling between the left NM lead and the central NM scattering region is

$$H_T = \sum_{k\sigma n} t_{k\sigma n} c_{k\sigma}^\dagger d_{n\sigma} + \text{H.c.} \quad (6)$$

Finally, the electron-magnon interaction between the right FI lead and the central scattering region is described by the  $s$ - $d$  exchange coupling [41,42]:

$$H_{sd} = - \sum_{qnm'} [J_{qnm'} d_{n\uparrow}^\dagger d_{n'\downarrow} a_q^\dagger + \text{H.c.}]. \quad (7)$$

$J_{qnm'}$  is the coupling strength of the scattering, in which a magnon in a FI is emitted with a spin-down electron at level  $n'$  scattered to a spin-up electron at level  $n$  in the central NM region, or vice versa. Although charge current cannot flow through the FI lead, the term  $J_{qnm'} d_{n\uparrow}^\dagger d_{n'\downarrow} a_q^\dagger$  allows a pure spin current mediated by magnons. As discussed in detail in Ref. [43], the momentum during the electron-magnon conversion is generally not conserved. However, the spin-nonconserving part of the Hamiltonian does not contribute to the spin transport and therefore can be neglected.

Note that all the Hamiltonians (3)–(7) are written in momentum space. To carry out tight-binding calculations, we need to discretize them in real space. For the convenience of presenting the potential landscape, we show here the discretization of Hamiltonian (5). Following procedures illustrated in Ref. [44], we get the matrix presentation of  $H_d$  as

$$[H_d]_{ij} = \begin{cases} V_i + 4t & \text{if } i = j, \\ -t & \text{if } i \text{ and } j \text{ are nearest neighbors,} \\ 0 & \text{otherwise.} \end{cases} \quad (8)$$

The matrix index  $i$  or  $j$  labels sites in the central region.  $t$  is the hopping parameter, and  $V_i$  is the on-site potential added to the central scattering region. In this work, we modify the potential landscape of three layers next to the interface in the central scattering region. Namely, in Eq. (8),

$$V_i = \begin{cases} v_1 & \text{for sites in layer 1,} \\ v_2 & \text{for sites in layer 2,} \\ v_3 & \text{for sites in layer 3,} \\ 0 & \text{otherwise.} \end{cases} \quad (9)$$

Considering the continuity condition for spin current in the system, the electronic spin current from the left NM lead should be equal to the magnonic spin current from the right FI lead, i.e.,  $I_{sL} = -I_{sR}$ , in which the subscript  $s$  denotes the spin

current while  $L(R)$  means the spin current is generated in the  $L(R)$  lead.

### A. dc spin current from the right lead

The spin current  $I_{sR}$  is calculated based on the Heisenberg equation  $I_{sR} = i[H_{sd}, \sum_q a_q^\dagger a_q]$ . Here, we find [45]

$$I_{sR}(t) = \int dt' \text{Tr} [G_\uparrow^r(t, t') \bar{\Sigma}_{R\uparrow}^<(t', t) + G_\uparrow^<(t, t') \bar{\Sigma}_{R\uparrow}^a(t', t) + \text{H.c.}], \quad (10)$$

where  $\bar{\Sigma}_{R\sigma}^r = iG_\sigma^r \cdot \bar{\Sigma}_{R\sigma}^< + iG_\sigma^< \cdot \bar{\Sigma}_{R\sigma}^a$ ,  $\bar{\Sigma}_{R\sigma}^< = iG_\sigma^< \cdot \bar{\Sigma}_{R\sigma}^>$ . We note that the electron-magnon self-energy  $\bar{\Sigma}_{R\sigma}$  is very similar to the electron-phonon [46] or electron-photon [47] self-energy, which contains the nonequilibrium Green's function of the system. The above equation is structurally the same as the current in normal systems except that the self-energy is replaced by the electron-magnon self-energy.

In the dc case, we find

$$I_{sR} = \int \frac{dE}{2\pi} \text{Tr} [G_\uparrow^r(E) \bar{\Sigma}_{R\uparrow}^<(E) + G_\uparrow^<(E) \bar{\Sigma}_{R\uparrow}^a(E) + \text{H.c.}], \quad (11)$$

where  $G_\uparrow^r(E) = 1/[g_{d\uparrow}^{-1}(E) - \Sigma_{L\uparrow}^r(E) - \bar{\Sigma}_{R\uparrow}^r(E)] = 1/[G_{L\uparrow}^{-1}(E) - \bar{\Sigma}_{R\uparrow}^r(E)]$ . After some algebra, Eq. (11) becomes [48]

$$I_{sR} = - \int dE \text{Tr} \{ G_\uparrow^r(E) \Gamma_{L\uparrow}(E) G_\uparrow^a(E) [i \bar{\Sigma}_{R\uparrow}^<(E) + 2f_{L\uparrow}(E) \text{Im} \bar{\Sigma}_{R\uparrow}^a(E)] \}. \quad (12)$$

The self-energy  $\bar{\Sigma}_{R\uparrow}$  has to be calculated self-consistently within the self-consistent Born approximation (SCBA). We first consider the Born approximation (BA) so that  $\bar{\Sigma}_{R\uparrow}^<(t, t') = iG_{L\downarrow}^<(t, t') \Sigma_R^>(t', t)$ . It is straightforward to show the following relation [49]:

$$\bar{\Sigma}_{R\uparrow}^<(E) = i \int d\omega [1 + f_R^B(\omega)] f_{L\downarrow}(\bar{E}) D_{L\downarrow}^0(\bar{E}) \Gamma_R(\omega), \quad (13)$$

where  $\bar{E} = E + \omega$ .  $f_R^B$  is the Bose-Einstein distribution for magnon gas in the right lead.  $D_{L\downarrow}^0(E) = G_{L\downarrow}^r(E) \Gamma_{L\downarrow}(E) G_{L\downarrow}^a(E)$  is the injectivity of the left lead, and an effective local DOS matrix for electrons coming from the left lead [50]. Here  $\Gamma_{L\downarrow} = \Gamma_{L\uparrow} = \Gamma_L = i(\Sigma_{L\downarrow}^r - \Sigma_{L\downarrow}^a)$  is the linewidth function of the left lead, and  $\Gamma_R = -2 \text{Im} \Sigma_R^r$ . Similarly, we find that the effective linewidth function of the right lead is given by [51]

$$\bar{\Gamma}_R(E) = \int d\omega [f_R^B(\omega) + f_{L\downarrow}(\bar{E})] D_{L\downarrow}^0(\bar{E}) \Gamma_R(\omega). \quad (14)$$

We emphasize that the self-energy  $\bar{\Sigma}_R^r$  and hence  $D_{L\downarrow}^0(\bar{E}) \Gamma_R(\omega)$  are nonzero only at the NM/FI interface. From Eqs. (13) and (14), we arrive at the final result,

$$I_{sR} = - \int d\omega [f_R^B(\omega) - f_{L\downarrow}^B(\omega)] \int dE [f_{L\uparrow}(E) - f_{L\downarrow}(E + \omega)] \text{Tr} [A_R(E, \omega)], \quad (15)$$

with

$$A_R(E, \omega) = G_{\uparrow}^r(E) \Gamma_{L\uparrow}(E) G_{\uparrow}^a(E) D_{L\downarrow}^0(\bar{E}) \Gamma_R(\omega) \quad (16)$$

and

$$\bar{\Sigma}_{R\uparrow}^r(E) = \int d\omega [f_R(\omega) G_{L\downarrow}^r(\bar{E}) + i f_{L\downarrow}(\bar{E}) \text{Im} G_{L\downarrow}^r(\bar{E})] \Gamma_R. \quad (17)$$

Note that we have used the identity

$$[f_{L\uparrow}(E) - 1] f_{L\downarrow}(\bar{E}) = -[f_{L\uparrow}(E) - f_{L\downarrow}(\bar{E})] f_L^B(\omega),$$

where  $f_{L\sigma}(\epsilon) = 1/[\exp(\beta_L(\epsilon - \mu_\sigma)) + 1]$ .  $f_L^B(\omega) = 1/[\exp(\beta_L(\omega + \mu_s)) - 1]$  is the effective Bose distribution of the left lead with the spin bias  $\mu_s = \mu_\uparrow - \mu_\downarrow$ .  $\beta_L = 1/k_B T_L$  is the inverse temperature of the left lead.  $\mu_\uparrow$  and  $\mu_\downarrow$  are chemical potentials for electrons in the left NM lead with spin up and down, which are set to  $\mu_\uparrow = \mu_\downarrow = \mu_L$  in our numerical calculations.

It is worth noting that when spin bias  $\mu_s$  and  $T_L - T_R$  are all zero, there is no spin current. In addition, if we keep only quadratic terms in coupling  $J_{qnn'}$  and treat Green's functions as scalars, Eq. (15) recovers the spin current found in a zero-dimensional system, which is consistent with previous results obtained from the equation of motion [7], the full counting statistics formalism [11], and nonequilibrium Green's function theory [14], respectively. For the spin current within the SCBA, Eq. (13) remains valid but one needs to iterate self-consistently to get a convergent  $\bar{\Sigma}_{R\uparrow}^r$  [45].

### B. Electron-magnon conversion

As shown in Eq. (12), if the right lead is replaced by a normal lead, i.e.,  $\Sigma_R^< = f_R(\Sigma_R^a - \Sigma_R^r)$  and  $\Sigma_R^a - \Sigma_R^r = i\Gamma_R$ , Eq. (12) would formally resemble the usual Landauer-Büttiker formula. In realistic systems, the electron-magnon coupling is usually very weak [41]. Nevertheless, it can be modified in a transport process. From Eq. (14), the effective self-energy of the FI lead is given by  $D_{L\downarrow}^0(\bar{E}) \Gamma_R(\omega)$ , which is proportional to the effective DOS at the NM/FI interface. Therefore, the effective electron-magnon coupling strength and the spin conductance can be enhanced by increasing the local DOS at the interface.

## III. NUMERICAL RESULTS

In numerical calculations, the spin bias  $\mu_s$  is set to zero. In the linear-response regime, we define the spin current driven by the temperature gradient  $\Delta T = T_L - T_R$  as  $I_{SR} = G_T \Delta T$ , in which  $G_T$  is the so-called spin conductance. We fix  $\Delta T = 0.001$  K to calculate the spin current using Eq. (15), and we present spin conductance in figures for discussion.

To perform numerical calculation for the spin current, we have to determine the self-energy  $\bar{\Sigma}_R^{r,<}$  defined in Eqs. (13) and (17). We assume that  $J_{qnn'} = J_q \delta_{nn'} \delta_{ni}$ , which corresponds to destroying a magnon and creating two electrons with opposite spins at the same lattice site at the interface. Index  $i$  denotes the level of interfacial site. We have

$$\bar{\Sigma}_{R\uparrow n_1 n}^r(\tau, \tau') = i\Gamma_0 G_{n_1 n \uparrow}^r(\tau, \tau') \Gamma_0 \Sigma_R(\tau', \tau), \quad (18)$$

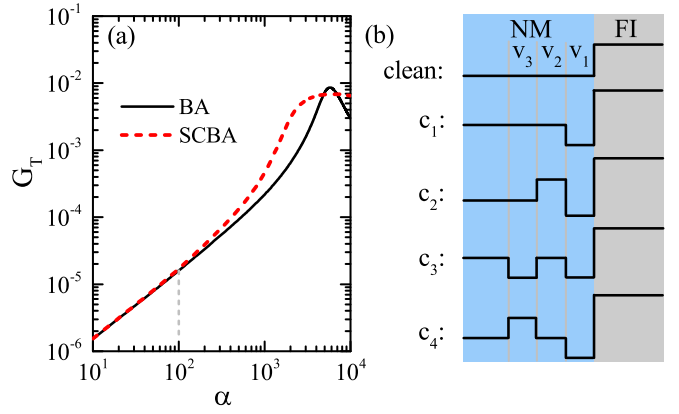


FIG. 3. (a) 2D spin conductance vs  $\alpha$  for the clean system in BA and SCBA. The parameter  $\alpha$  is the dimensionless coupling in an Ohmic spectral function. The temperature is fixed at  $T = 5$  K and the Fermi energy of the left NM lead is  $\mu_L = 0.8$  meV. In the following calculations,  $\alpha$  is fixed to 100, which is labeled by the gray dashed line. The spin conductance  $G_T$  is in units of meV/K. (b) Schematic of on-site potential ( $v_3, v_2, v_1$ ) for a clean system and four typical configurations.  $c_1 - c_4$ :  $(0, 0, -v)$ ;  $(0, v, -v)$ ;  $(-v, 0, -v)$ ;  $(v, 0, -v)$ .

where  $\Gamma_0$  is a diagonal matrix with nonzero matrix elements at the interface of the right lead and  $\Sigma_R(\tau, \tau') = \sum_q J_q^2 g_{Rq}(\tau, \tau')$ .

Since the FI lead is always in equilibrium, we follow other theoretical investigations in the FI [7,11,14,52] and assume that the spectral function of the magnonic reservoir is Ohmic so that

$$\Gamma_R(\omega) = \alpha \omega e^{-\omega/\omega_c} t \Gamma_0, \quad (19)$$

where  $\alpha \sim J_q^2$  is the dimensionless effective coupling energy between NM and FI.  $\omega_c$  is the cutoff frequency used to truncate the Ohmic spectrum in high frequency. As discussed in Ref. [41],  $\alpha$  is related to the spin-mixing conductance [10,53]. Another choice of  $\Gamma_R$  will not change the results qualitatively.

In the numerical calculation, we use a tight-binding approach to discretize the 2D and 3D systems [44]. The self-energy of the left lead is calculated using the transfer-matrix method [54], from which the Green's function  $G_{L\downarrow}^r$  can be calculated. Once  $G_{L\downarrow}^r$  is obtained,  $\bar{\Sigma}_{R\uparrow}^r$  and  $G_{\uparrow}^r$  can also be calculated. Finally, one has to perform a double integration over energy and frequency for spin conductance, which is very time-consuming.

### A. Enhancement of spin conductance

We consider a 2D system using a  $20 \times 20$  mesh with lattice spacing  $a = 5$  nm so that the hopping parameter  $t = 21.8$  meV. We consider the ballistic regime and set the potential of the NM regime to be a constant. We fix the temperature  $T = 5$  K,  $\omega_c = 0.24$  meV, and  $\mu_L = 0.8$  meV, which corresponds to the first subband transport. As will be seen below, the enhancement effect mainly comes from the first subband transport.

Since we consider the ballistic regime, the material ingredients are manifested in the electron-magnon coupling constant. In Fig. 3(a), the 2D spin conductance versus  $\alpha$  is depicted for the clean system ( $v = 0$ ) using BA and SCBA, which shows a



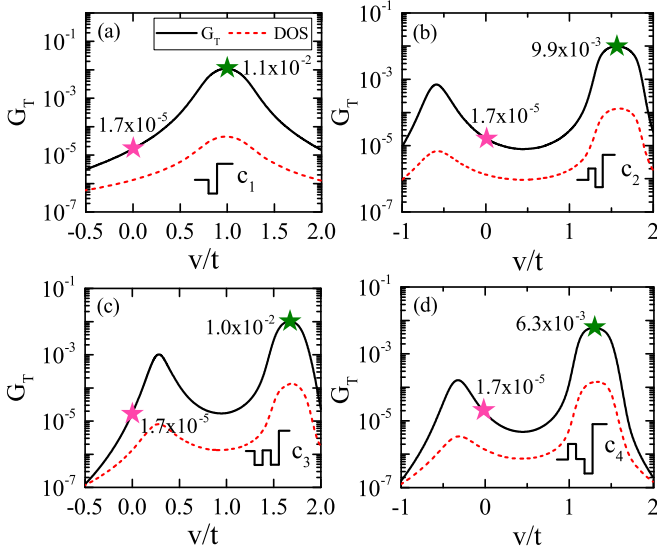


FIG. 4. 2D spin conductance (solid line) and the corresponding effective interfacial DOS (dashed line) vs  $v$  for different configurations  $c_1$ – $c_4$  [in panels (a)–(d)] in SCBA at  $\alpha = 100$ . The pink star is the reference with no interfacial modification, while the green star shows the largest enhancement. Insets: potential profiles for the corresponding configurations.  $G_T$  is in units of meV/K. Parameters:  $\alpha = 100$ ,  $\mu_L = 0.8$  meV,  $T = 5$  K, and  $t = 21.8$  meV.

nonmonotonic dependence. The maximum spin conductance is about  $7 \times 10^{-3}$  at  $\alpha > 2500$  in SCBA, setting up an upper bound for the chosen system parameters. We choose here the most popular (optimal) NM/FI interface, Pt/YIG, as an example with a suitable parameter  $\alpha$  ( $\alpha = [100, 1000]$ ) that is within the estimated range of electron-magnon coupling for that interface. We choose  $\alpha = 100$  such that the self-energy  $\bar{\Sigma}_R^r$  is in the order of magnon energy (less than  $k_B T$ ), which is equivalent to  $\eta = 1$ .  $\eta$  is the effective coupling constant at the Pt-YIG interface defined in Ref. [41].

To change the interfacial DOS, We consider four typical configurations (from  $c_1$  to  $c_4$ ):  $(v_3, v_2, v_1) = (0, 0, -v)$ ;  $(0, v, -v)$ ;  $(-v, 0, -v)$ ;  $(v, 0, -v)$ . Here,  $v$  denotes the potential strength, which is in units of hopping parameter  $t$ . Figure 3(b) shows the configuration potentials for  $v > 0$ . Taking the work function of the left NM lead (or the central region) as zero potential, an applied positive potential on the three interfacial layers corresponds to the insertion of a material with higher work function, while a negative potential corresponds to the insertion of a material with lower work function. They can be classified into three categories: one-layer configuration ( $c_1$ ), two-layer configuration ( $c_2$ ), and three-layer configurations ( $c_3$  and  $c_4$ ). For each configuration, we calculate the spin conductance  $G_T$  as a function of  $v$  in SCBA and compare it to the spin conductance of a clean system. For the clean system, SCBA gives  $G_T = 1.7 \times 10^{-5}$  meV/K (pink star in Fig. 4), which is the reference for the enhancement of spin conductance. We note that in principle, the same effect may be obtained by applying a gate voltage if one can control the applied gate voltage precisely. However, this could be very difficult in practice, especially for complex configurations such as  $c_3$  and  $c_4$ .

## B. One-layer strategy

A one-layer configuration corresponds to the insertion of one “layer” of intermediate material at the Pt-YIG interface. For the  $c_1$  configuration, we set  $(v_3, v_2, v_1) = (0, 0, -v)$ . The spin conductance and corresponding effective interfacial DOS versus  $v$  within the SCBA are shown in Fig. 4(a). In this work, the effective interfacial DOS is defined as

$$\bar{\rho} = \int dE \int d\omega (f_R^B(\omega) + f_{L\downarrow}(\bar{E})) D_{L\downarrow}^0(\bar{E}) \Gamma_R(\omega). \quad (20)$$

We see that the spin conductance and the corresponding effective interfacial DOS are well correlated. This indicates that the increase of the interfacial DOS is the microscopic mechanism of the enhancement in spin conductance. When the potential  $v$  is tuned to an appropriate value, electrons near the interface can be transported due to the quasibound states above the potential well. This leads to a significant increase in the interfacial DOS, which further enhances the effective coupling between the central NM region and the FI lead. The spin conductance is thus enhanced significantly. In addition, spin conductance enhancement occurs when the intermediate layer has a lower work function than that of Pt (corresponding to positive  $v$ ). For configuration  $c_1$ , the largest enhancement can reach 647 times [compare the green star and the pink star in Fig. 4(a)]. On the other hand, inserting an intermediate material with a higher work function (corresponding to negative  $v$ ) suppresses the spin conductance. Our result is consistent with experimental results showing that an enhancement between 300% and 600% was achieved when intermediate materials such as Ru [18], monolayer WSe<sub>2</sub> [23], multilayer MoS<sub>2</sub> [25,26], and C<sub>60</sub> [24] were inserted at the Pt-YIG interface [55]. The enhancement has previously been attributed to the reduction of conductivity mismatch at the Pt/YIG interface, i.e., the spin-mixing conductance  $g_{\text{Pt/YIG}}$  is smaller than the total conductance of Pt/X/YIG trilayer [56]. Since interfacial conductance has been considered implicitly in the potential profile of the TB model, we interpret it as being due to the enhancement of the effective interfacial DOS [57]. Moreover, when a nanoscale amorphous layer is formed at the interface [19] or the interface is oxidized [18], the spin conductance is suppressed [58], which is also consistent with our result.

## C. Two-layer strategy

Figure 4(b) shows the spin conductance and effective interfacial DOS as a function of  $v$  for a “two-layer” configuration, i.e.,  $(v_3, v_2, v_1) = (0, v, -v)$ , where two different materials are required to insert into the interface. When  $v$  is negative, a factor of 44 enhancement can be obtained. When  $v$  is positive, a potential barrier is created followed by a potential well near the interface [see the inset of Fig. 4(b)]. As a result, an incident electron can dwell inside the well for a long time, giving rise to a very large DOS at the interface. The enhancement of the spin conductance is calculated to be 582 times. It is clear that adding a potential barrier increases the interfacial conductivity mismatch. Since the conductance mismatch at the NM/FI interface can be viewed as a “potential barrier” at the interface, introducing a second barrier in the configuration  $c_2$  demonstrates the importance of the “double-barrier” structure, which has not yet been explored experimentally.

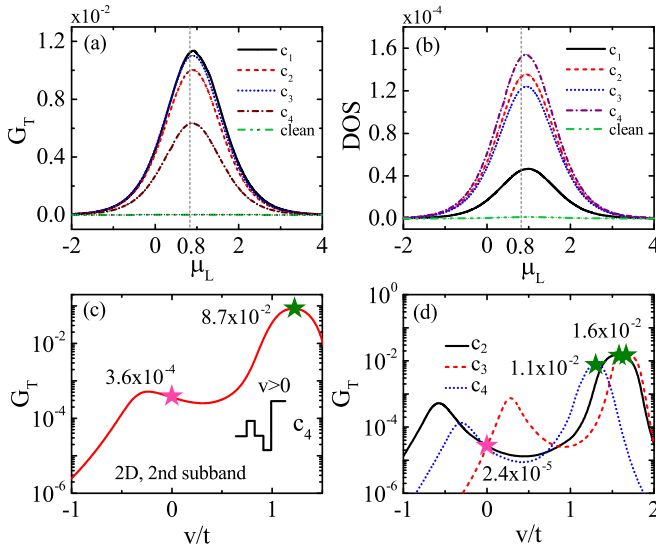


FIG. 5. Contributions of the first subband to the (a) 2D spin conductance and (b) effective interfacial DOS as a function of Fermi energy  $\mu_L$  (in units of meV). The potential strengths  $v$  for  $c_1 - c_4$  are fixed at values labeled by green stars in Fig. 4, i.e.,  $v/t = \{1, 1.58, 1.64, 1.3\}$ , respectively. (c) 2D spin conductance vs  $v$  for configuration  $c_4$  when the incident electron is in the second subband, yielding a maximum of 242 enhancement. (d) 3D spin conductance vs  $v$  for configurations  $c_2 - c_4$  when the incident electron is in the first subband. The enhancement is about 708, 708, and 416 times, respectively, for  $c_2 - c_4$ . Here the system is a nanowire with a cross-section  $20 \times 20$  and  $\alpha = 100$ .  $G_T$  is in units of meV/K.

#### D. Three-layer strategy

Figures 4(c) and 4(d) depict the spin conductance and effective interfacial DOS versus  $v$  for configurations  $c_3$  and  $c_4$ . The configuration  $c_3$  is a double-well structure, and an enhancement of 588 times can be achieved. The configuration  $c_4$  corresponds to a “double-barrier” structure similar to  $c_2$ . As expected from the result of  $c_2$ , a large enhancement of 371 times is obtained.

Note that the largest enhancement occurring at a particular potential parameter in  $c_1 - c_4$  is a direct consequence of enhancement in the effective interfacial DOS. We show in Figs. 5(a) and 5(b) the spin conductance and effective interfacial DOS as a function of Fermi energy. The potential strengths  $v$  for  $c_1 - c_4$  are fixed at the resonance points labeled by green stars in Fig. 4, respectively. The spin conductance and effective interfacial DOS of  $c_1 - c_4$  show clearly peaks near the Fermi energy  $\mu_L = 0.8$  meV compared to a clean system. If an incident electron has two transmission channels, the longitudinal energies of each channel are different [59]. Therefore, only one of the transmission channels can reach resonance. As a result, the largest enhancement is expected to reduce by a factor of 2, which is confirmed numerically [reduced from 371 times to 242 times; see Fig. 5(c) compared to Fig. 4(d)]. This shows that the giant enhancement of spin conductance is prominent only in the first subband transport. A giant enhancement of spin conductance 708 times in a 3D nanowire NM/NM/FI system is also achieved when an incoming electron is in the first subband [see Fig. 5(d)].

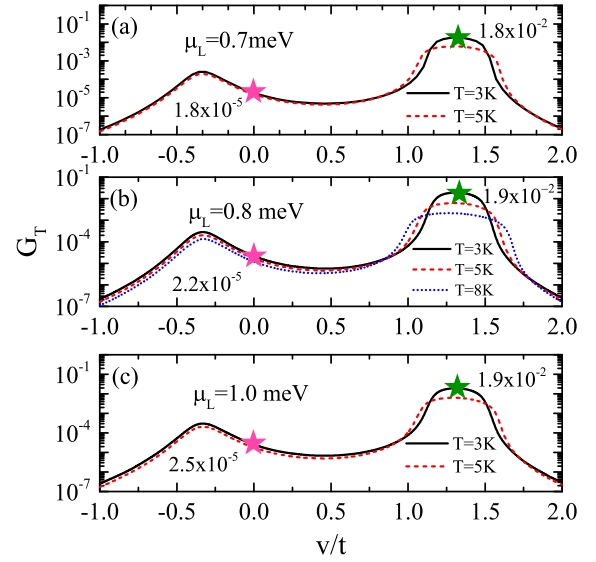


FIG. 6. 2D spin conductance vs  $v$  for configuration  $c_4$  at different temperatures and Fermi energies (a)  $\mu_L = 0.7$  meV, (b)  $\mu_L = 0.8$  meV, and (c)  $\mu_L = 1.0$  meV. The configuration for  $c_4$  is  $(v, 0, -v)$ ,  $\alpha = 100$ .  $G_T$  is in units of meV/K.

We point out that our model calculation is carried out in a 2D nanoribbon and 3D nanowire within the TB approach, and it may not be applicable directly to realistic systems. In addition, the enhancement effect is prominent only in the first subband. Nevertheless, our theory provides a physical understanding of the enhancement of magnon-mediated spin conductance, and general theoretical guidance for interface engineering of effective electron-magnon coupling. Although a large enhancement of spin conductance is obtained theoretically in this work, it is still a challenging task for experiments.

In this work, in addition to the Born approximation we also make an approximation on static electron-magnon coupling, neglecting the dipole-dipole interaction in the FI and a possible dephasing mechanism. We note that the enhancement of effective electron-magnon coupling is on top of the static electron-magnon coupling, so the approximation made on static electron-magnon coupling does not matter. In addition, the enhancement is due to the increase of the local DOS in the neighborhood of the NM/FI interface where dephasing can be neglected. Furthermore, as shown in Fig. 6, an enhancement of 760–1000 times is achieved for configuration  $c_4$  by varying different Fermi energies and temperatures. The large enhancement of 2D spin conductance does not depend on Fermi energies and temperatures, suggesting that it is a generic feature.

#### IV. CONCLUSION

We have developed a theoretical formalism based on the nonequilibrium Green’s function method for magnon-mediated spin current in an NM/NM/FI heterostructure. Because the electron-magnon conversion across the NM/FI interface is a nonlinear process, the effective electron-magnon coupling of the NM/FI interface is an energy convolution

of the local DOS of the system with the spectral function of the FI lead, in distinct contrast to normal systems. Given that the electron-magnon coupling is very weak, this provides a new possibility to manipulate the coupling by modifying the potential landscape near the interface. As demonstrated in this work, simple modification of the interfacial DOS can drastically increase the spin conductance in both 2D and 3D

systems as a result of enhancement of effective electron-magnon coupling.

### ACKNOWLEDGMENTS

This work was financially supported by the Natural Science Foundation of China (Grant No. 12034014).

- 
- [1] Y. Kajiwara, K. Harii, S. Takahashi, J. Ohe, K. Uchida, M. Mizuguchi, H. Umezawa, H. Kawai, K. Ando, K. Takanashi, S. Maekawa, and E. Saitoh, *Nature (London)* **464**, 262 (2010).
- [2] D. Wesenberg, T. Liu, D. Balzar, M. Z. Wu, and B. L. Zink, *Nat. Phys.* **13**, 987 (2017).
- [3] H. Adachi, K. Uchida, E. Saitoh, and S. Maekawa, *Rep. Prog. Phys.* **76**, 036501 (2013).
- [4] A. Brataas, B. V. Wees, O. Klein, G. D. Loubens, and M. Viret, *Phys. Rep.* **885**, 1 (2020).
- [5] J. Xiao, G. E. W. Bauer, K. C. Uchida, E. Saitoh, and S. Maekawa, *Phys. Rev. B* **81**, 214418 (2010).
- [6] H. Adachi, J. I. Ohe, S. Takahashi, and S. Maekawa, *Phys. Rev. B* **83**, 094410 (2011).
- [7] J. Ren, *Phys. Rev. B* **88**, 220406(R) (2013).
- [8] Y. Ohnuma, M. Matsuo, and S. Maekawa, *Phys. Rev. B* **96**, 134412 (2017).
- [9] M. Matsuo, Y. Ohnuma, T. Kato, and S. Maekawa, *Phys. Rev. Lett.* **120**, 037201 (2018).
- [10] Y. Tserkovnyak, A. Brataas, and G. E. W. Bauer, *Phys. Rev. Lett.* **88**, 117601 (2002).
- [11] G. M. Tang, X. B. Chen, J. Ren, and J. Wang, *Phys. Rev. B* **97**, 081407(R) (2018).
- [12] B. Sothmann and M. Buttiker, *Europhys. Lett.* **99**, 27001 (2012).
- [13] L. Karwacki, P. Trocha, and J. Barnas, *Phys. Rev. B* **92**, 235449 (2015).
- [14] L. Gu, H. H. Fu, and R. Q. Wu, *Phys. Rev. B* **94**, 115433 (2016).
- [15] Steven S.-L. Zhang and S. Zhang, *Phys. Rev. Lett.* **109**, 096603 (2012).
- [16] H. Wu, C. H. Wan, X. Zhang, Z. H. Yuan, Q. T. Zhang, J. Y. Qin, H. X. Wei, X. F. Han, and S. Zhang, *Phys. Rev. B* **93**, 060403(R) (2016).
- [17] Y. Ohnuma, H. Adachi, E. Saitoh, and S. Maekawa, *Phys. Rev. B* **87**, 014423 (2013).
- [18] F. Nakata, T. Niimura, Y. Kurokawa, and H. Yuasa, *Jpn. J. Appl. Phys.* **58**, 090602 (2019).
- [19] Z. Qiu, K. Ando, K. Uchida, Y. Kajiwara, R. Takahashi, H. Nakayama, T. An, Y. Fujikawa, and E. Saitoh, *Appl. Phys. Lett.* **103**, 092404 (2013).
- [20] A. Aqeel, I. J. Vera-Marun, B. J. van Wees, and T. T. M. Palstra, *J. Appl. Phys.* **116**, 153705 (2014).
- [21] F. Hellman, A. Hoffmann, Y. Tserkovnyak, G. S. D. Beach, E. E. Fullerton, C. Leighton, A. H. MacDonald, D. C. Ralph, D. A. Arena, H. A. Durr, P. Fischer, J. Grollier, J. P. Heremans, T. Jungwirth, A. V. Kimel, B. Koopmans, I. N. Krivorotov, S. J. May, A. K. Petford-Long, J. M. Rondinelli *et al.*, *Rev. Mod. Phys.* **89**, 025006 (2017).
- [22] X. Jia, K. Liu, K. Xia, and G. E. W. Bauer, *Europhys. Lett.* **96**, 17005 (2011).
- [23] S. K. Lee, W. Y. Lee, T. Kikkawa, C. T. Le, M. S. Kang, G. S. Kim, A. D. Nguyen, Y. S. Kim, N. W. Park, and E. Saitoh, *Adv. Funct. Mater.* **30**, 2003192 (2020).
- [24] V. Kalappattil, R. Geng, R. Das, M. Pham, H. Luong, T. Nguyen, A. Popescu, L. M. Woods, M. Klaui, H. Srikanth, and M. H. Phan, *Mater. Horizons* **7**, 1413 (2020).
- [25] W. Y. Lee, N. W. Park, M. S. Kang, G. S. Kim, H. W. Jang, E. Saitoh, and S. W. Lee, *J. Phys. Chem. Lett.* **11**, 5338 (2020).
- [26] W. Y. Lee, N. W. Park, G. S. Kim, M. S. Kang, J. W. Choi, K. Y. Choi, H. W. Jang, E. Saitoh, and S. W. Lee, *Nano Lett.* **21**, 189 (2021).
- [27] H. L. Wang, C. H. Du, P. C. Hammel, and F. Y. Yang, *Phys. Rev. Lett.* **113**, 097202 (2014).
- [28] W. W. Lin, K. Chen, S. F. Zhang, and C. L. Chien, *Phys. Rev. Lett.* **116**, 186601 (2016).
- [29] M. Büttiker, *J. Phys.: Condens. Matter* **5**, 9361 (1993).
- [30] J. Wang, H. Guo, J. L. Mozos, C. C. Wan, G. Taraschi, and Q. R. Zheng, *Phys. Rev. Lett.* **80**, 4277 (1998).
- [31] J. G. Hou, B. Wang, J. L. Yang, X. R. Wang, H. Q. Wang, Q. S. Zhu, and X. D. Xiao, *Phys. Rev. Lett.* **86**, 5321 (2001).
- [32] To be more precise, this DOS is defined as the local density of states for an electron coming from a particular lead [29], and it is also called injectivity.
- [33] G. Breit and E. Wigner, *Phys. Rev.* **49**, 519 (1936).
- [34] A. D. Stone and P. A. Lee, *Phys. Rev. Lett.* **54**, 1196 (1985).
- [35] R. G. Newton, *Scattering Theory of Waves and Particles* (McGraw Hill, New York, 1966), Chap. 16.
- [36] S. Datta, *Electronic Transport in Mesoscopic Systems* (Cambridge University Press, New York, 1995), Chap. 6.
- [37] A. Uma Maheswari, P. Prema, S. Mahadevan, and C. S. Shastri, *Pramana* **73**, 969 (2009).
- [38] A. Uma Maheswari, P. Prema, and C. S. Shastri, *Am. J. Phys.* **78**, 412 (2010).
- [39] C. A. Moyer, *AIP Adv.* **4**, 027109 (2014).
- [40] T. Holstein and H. Primakoff, *Phys. Rev.* **58**, 1098 (1940).
- [41] J. S. Zheng, S. Bender, J. Armaitis, R. E. Troncoso, and R. A. Duine, *Phys. Rev. B* **96**, 174422 (2017).
- [42] In obtaining Hamiltonian  $H_R$ , we start from the Heisenberg model and make a Holstein-Primakoff transformation [40]. Hence there is an extra factor  $\sqrt{2S_0}$  associated with  $a_q$  and  $a_q^\dagger$  in  $H_{sd}$ , which is dropped for the moment. Here  $S_0$  is the length of the lattice spin.
- [43] S. A. Bender, R. A. Duine, and Y. Tserkovnyak, *Phys. Rev. Lett.* **108**, 246601 (2012).

- [44] S. Datta, *Electronic Transport in Mesoscopic Systems* (Cambridge University Press, New York, 1995), Chap. 3.
- [45] G. Li, H. Jin, Y. Wei, and J. Wang, [arXiv:2112.11021](https://arxiv.org/abs/2112.11021).
- [46] R. Lake and S. Datta, *Phys. Rev. B* **45**, 6670 (1992).
- [47] J. Z. Chen, Y. B. Hu, and H. Guo, *Phys. Rev. B* **85**, 155441 (2012).
- [48] From now on, we absorb  $1/(2\pi)^2$  from  $dE$  and  $d\omega$  into the unit of spin current. To resume the correct unit, the factor of  $S_0/(4\pi^2\hbar)$  should be multiplied in calculating spin current.
- [49] For fermions,  $\Sigma_\alpha^< = if_\alpha\Gamma_\alpha$  and  $\Sigma_\alpha^> = i(f_\alpha - 1)\Gamma_\alpha$ . For bosons,  $\Sigma_\alpha^< = -if_\alpha\Gamma_\alpha$  and  $\Sigma_\alpha^> = -i(f_\alpha + 1)\Gamma_\alpha$ .
- [50] T. Christen and M. Buttiker, *Phys. Rev. Lett.* **77**, 143 (1996).
- [51] We have used the relation  $G^r - G^a = -iG^r\Gamma G^a$ , which means that  $\text{Im}G^r < 0$ .
- [52] U. Weiss, *Quantum Dissipative Systems* (World Scientific, Singapore, 2012).
- [53] A. Brataas, Yu. V. Nazarov, and G. E. W. Bauer, *Phys. Rev. Lett.* **84**, 2481 (2000).
- [54] M. P. Lopez-Sancho *et al.*, *J. Phys. F* **14**, 1205 (1984); **15**, 851 (1985).
- [55] We note that the work function of Pt is almost the largest among metals and semiconductors. Therefore, insertion of an intermediate layer of metals or semiconductors amounts to putting in a potential well.
- [56] The reduction of conductivity mismatch can be estimated by comparing  $g_{\text{Pt/YIG}}^{-1}$  with  $g_{\text{Pt/X}}^{-1} + g_{\text{X/YIG}}^{-1} + G_X^{-1}$ , where  $g_{\text{Pt/X}}$  and  $g_{\text{X/YIG}}$  are spin-mixing conductances of Pt/X and X/YIG interfaces, respectively, and  $G_X$  is the conductance of the X layer. It is clearly a sequential picture in quantum transport.
- [57] Inserting a different material at the Pt/YIG interface leads to a change in  $\alpha$ , which we have neglected.
- [58] This corresponds to a negative  $v$  in Fig. 4(a), which suppresses the spin conductance.
- [59] Since  $E = (n\pi/a)^2 + k_n^2$ , different subbands have different longitudinal energies.